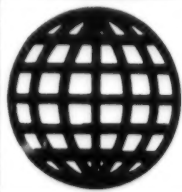


JPRS-CST-92-019

13 OCTOBER 1992



**FOREIGN
BROADCAST
INFORMATION
SERVICE**

JPRS Report

Science & Technology

China

SCIENCE & TECHNOLOGY

CHINA

CONTENTS

LASERS, SENSORS, OPTICS

Reports on Pulsed Power Research.....	1
High-Voltage Steep-Pulse Generator [Wang Xiaojun, Chen Ping, et al.; QIANG JIGUANG YU LIZI SHU, May 92]..	1
3-cm Relativistic Backward-Wave Oscillator [Li Jiayin, Yu Shanfu, et al.; QIANG JIGUANG YU LIZI SHU, May 92]..	6
High-Performance Short-Period FEL Wiggler [Li Qingxiang, Zhou Chuanming, et al.; QIANG JIGUANG YU LIZI SHU, May 92].....	15

MICROELECTRONICS

Design of Electron Optical Column for DJ-2 Variable-Rectangle E-Beam Lithography System With 0.2-Micron Edge Resolution [Kang Niankan; DIANZI KEXUE XUEKAN, Mar 92].....	21
--	----

Reports on Pulsed Power Research

High-Voltage Steep-Pulse Generator

92FE0732A Chengdu QIANG JIGUANG YU LIZI SHU [HIGH POWER LASER AND PARTICLE BEAMS] in Chinese Vol 4 No 2, May 92 pp 228-232

[Article by Wang Xiaojun [3769 0879 6511], Chen Ping [7115 1627], Yang Dawei [2799 1129 3634] and Zeng Naigong [2582 0035 1562] of China Institute of Atomic Energy, P.O. Box 275, Slot 7, Beijing 102413: "High-Voltage Steep-Pulse Generator"; MS received 19 Jul 91, Revised 19 Nov 91]

[Text] Abstract

The discharge circuit of a Marx generator is analyzed in this paper and a calculation program is given. In addition, a high-voltage steep-pulse generator with an output voltage of 160 kV and a rise time of less than 5 ns is designed and constructed on the basis of this theoretical analysis.

I. Introduction

In recent years, high-voltage steep-pulse technology has attracted a great deal of attention because a high-voltage steep-pulse generator can release a tremendous amount of energy in a very short period of time. It not only requires a high output voltage but also a steep rise time. These two requirements are often contradictory. With increasing pulse voltage and current, the generator must also increase in size. This causes the loop inductance and parasitic capacitance to rise as well. Discharge loop inductance and parasitic capacitance are major factors affecting the rise time of the waveform. Most generators available today (such as the models TG-70 and TG-125 manufactured by the P.I. Co. in the United States and the Maxwell Co.'s model 40151) are at approximately 10 kV/ns. As a trigger for a switch, the voltage gradient has a direct impact on the performance of the switch. The larger the gradient, the smaller the turn-on time and flutter and the more stable the switch. For instance, a very high voltage gradient is required as a power supply for a pumped laser, or a high voltage standard power supply for a measuring system. In this work, on the basis of a computer analysis of the discharge circuit, a high-voltage steep-pulse generator with an output voltage of 160 kV and a rise time of under 10 ns is designed and constructed as the spark-gap trigger for an intense current accelerator.

II. Theoretical Analysis of the Discharge Loop of Marx Generator

Although there are several ways to produce a high-voltage steep pulse, the most common method is to use the discharge of a Marx generator. Figure 1 shows its equivalent circuit.

C_m : Main capacitance
 L_m : Circuit inductance
 R_A : Load resistance
 R_s : Circuit resistance
 C_B : Load capacitance

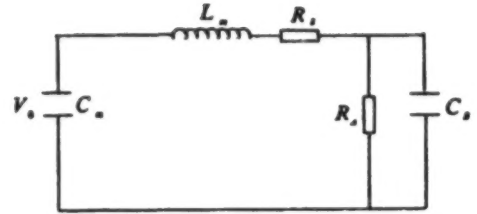


Figure 1. Equivalent Circuit of Marx Generator Discharge

The Laplace-transformed expression for the output voltage can be derived by performing a Laplace transformation on the equation of the discharge circuit:

$$V_B(s) = V_0 \omega_B^2 [s^3 + (\frac{1}{\tau_1} + \frac{1}{\tau_2})s^2 + (\omega^2 + \frac{1}{\tau_1 \tau_2})s + \frac{\omega_m^2}{\tau_2}]^{-1}$$

where $\omega_B = \frac{1}{\sqrt{L_m C_B}}$; $\omega_m = \frac{1}{\sqrt{L_m C_m}}$

$$\tau_1 = \frac{L_m}{R_s}; \quad \tau_2 = R_A C_B; \quad \omega = \sqrt{\omega_R^2 + \omega_m^2}$$

The inverse Laplace transform of $V_B(s)$ can be written as

$$V_B(t) = V_0 \omega_B^2 \left[\frac{e^{s_1 t}}{(s_1 - s_2)(s_1 - s_3)} + \frac{e^{s_2 t}}{(s_2 - s_1)(s_2 - s_3)} + \frac{e^{s_3 t}}{(s_3 - s_1)(s_3 - s_2)} \right]$$

where s_1 , s_2 , and s_3 are the roots of equation (1):

$$s^3 + (\frac{1}{\tau_1} + \frac{1}{\tau_2})s^2 + (\omega^2 + \frac{1}{\tau_1 \tau_2})s + \frac{\omega_m^2}{\tau_2} = 0 \quad (1)$$

Equation (1) is solved by computer and the result is substituted back into the expression for $V_B(t)$ and the value of V_B at any given time is known. With given values of V_0 , R_A and C_m , by plugging in different L_m , C_B and R_s , the leading edges of L_m and C_B as a function of rise time τ_s are as shown in Figures 2 and 3, respectively.

From Figures 2 and 3, loop inductance and load capacitance almost have the same effect on the rise time. In order to keep the rise time below 10 ns, we must have $C_B \leq 10$ pF and $L_m \leq 0.3$ μ H. The calculation also shows that although R_s does not affect the rise time, it has an impact on the output voltage efficiency. Furthermore, it also affects the amplitude of oscillation. The larger R_s is, the lower the voltage output efficiency becomes. Nevertheless, the overshoot is also less.

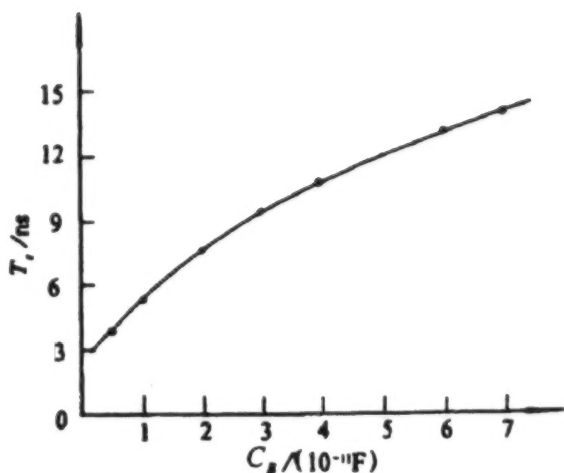


Figure 2. Curve of Rise-Time Vs. Load Capacitance

$C_m = 1.425 \text{ nF}$; $V_0 = 160 \text{ kV}$; $R_A = 500 \Omega$; $R_s = 45 \Omega$; $L_m = 0.3 \mu\text{H}$

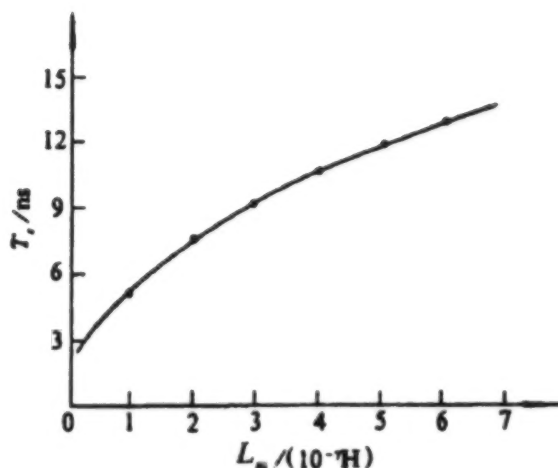


Figure 3. Curve of Rise-Time Vs. Loop Inductance

$C_B = 30 \text{ pF}$; $V_0 = 160 \text{ kV}$; $R_A = 500 \Omega$; $R_s = 45 \Omega$; $L_m = 0.3 \mu\text{H}$; $C_m = 1.425 \text{ nF}$

III. Generator Design and Estimation of Parameters

Based on the above calculation, we know that loop inductance and load capacitance are the primary factors affecting the rise time of a generator. Hence, L_m and C_B ought to be kept as small as possible. This also means that the size of the generator should be reduced to the extent possible as long as voltage resistance can be ensured. There are three common methods: 1) oil immersion, 2) gas filling, and 3) vacuum. When the generator is not very large, it is usually gas-filled. In our design, in addition to gas filling, the following measures are taken to improve the output waveform: 1) using coaxial symmetric configuration, 2) selecting low-inductance ceramic capacitors, and 3) employing larger-diameter ring-shaped electrodes. Hence, the loop inductance is further reduced. In addition, a coaxial multi-stage trigger scheme and a high-performance pre-trigger are used to reduce the scatter in the output voltage waveform. Figure 4 shows the schematic diagram of the Marx generator.

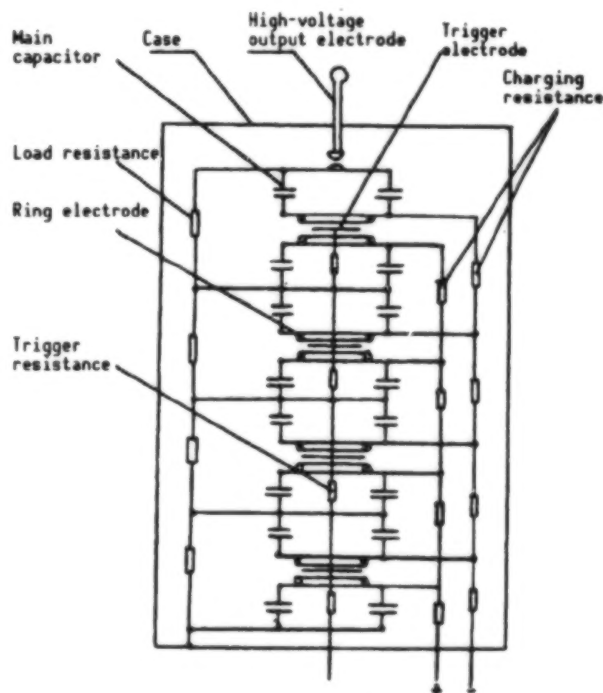


Figure 4. Schematic Diagram of Marx Generator

Parameters of the discharge loop (such as inductance, load capacitance and loop resistance) are not constants and they are difficult to calculate

accurately. It is only possible to estimate that loop inductance is a function of spark channel inductance, main capacitor inductance, electrode capacitance and high-voltage output electrode inductance. Since low-inductance capacitors and flat electrodes are used in our design, loop inductance is primarily determined by the inductance of the spark channel and high-voltage output electrode. It is estimated that the overall loop inductance is approximately 185 nH. Load capacitance is a combination of the stray capacitance between the high-voltage output to ground and that of the measurement devices (e.g., voltage dividers). The total load capacitance is estimated to be about 20 pF. The discharge loop resistance is comprised of spark resistance, electrode resistance and various contact resistance. Because of the small size, the load capacitance of our device is low. Consequently, the spark resistance is relatively large in comparison. Hence, contact resistance and electrode resistance can be neglected. From the standpoint of high-voltage output efficiency, spark resistance should be minimized. Therefore, the device should be operated under high pressure at high voltage.

After inputting the parameters into a computer, the output waveform is as shown in Figure 5.

The rise time is $T_s \approx 6.0$ ns and the output voltage is $V_B = 163$ kV. Based on the calculation, the parameters of the generator have met our design requirements.

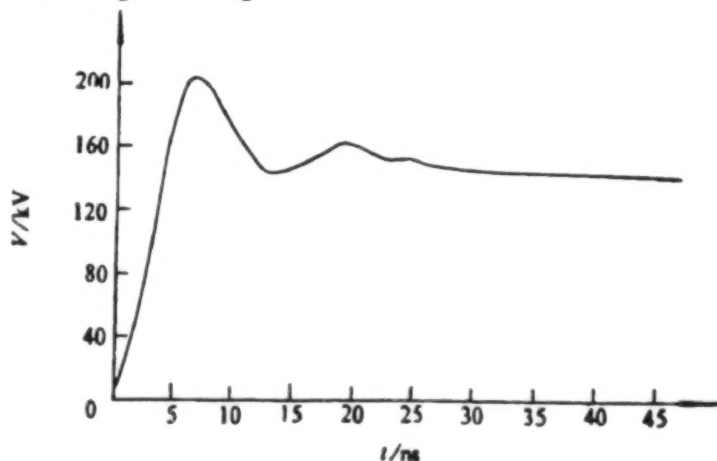


Figure 5. Curve of Output Voltage Vs. Time
 $C_m = 1.425$ nF; $R_A = 500\Omega$; $V_0 = 190$ kV;
 $L_m = 185$ nF; $C_B = 20$ pF; $R_S = 50\Omega$

IV. Experimental Results

After the generator was assembled, the suitable gap and pressure were selected experimentally. The gas used is nitrogen and the pressure is 0.1 MPa–0.25 MPa. The capacitor is charged to 9 kV–25.5 kV. The oscilloscope is an OK-19 100 MHz high-voltage oscilloscope. Figure 6 shows a series of oscillograms. As one can see, the overshoot is significantly increased with rising voltage. This is due to a decrease in the spark resistance.

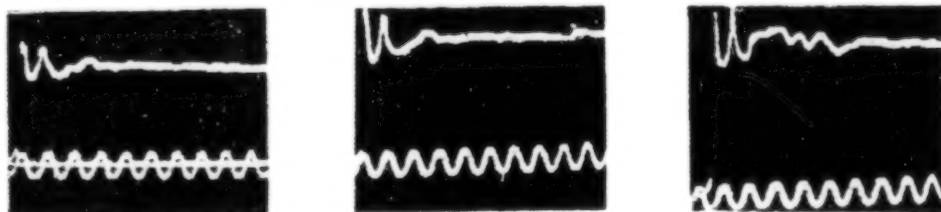


Figure 6. Typical Oscillograms

Table 1. Voltage Gradient Vs. Output Voltage

V_{out}/kV	74.1	114.7	125.0	138.0	144.3	150.0	161.5	173.4	178.7
$dV/dt/(kV \cdot ns^{-1})$	22.5	29.5	32.6	30.4	37.2	42.5	45.9	46.3	48.7

After processing a great deal of waveform data, one realizes that the output voltage gradient increases with rising voltage, as shown in Table 1. This is because the electric field between electrodes also increases as voltage rises, which shortens the discharge time.

Figure 7 shows the histogram and statistical probability density distribution of the waveform rise time (i.e., the time it takes the voltage to rise from 0 to its maximum value). The maximum distribution value is $\bar{T}_r \approx 4.79$ ns, the standard deviation is $\sigma = 0.65$ ns and the statistical number is $N = 89$.

A comparison of the experimental data to the theoretical calculation shows that the measured rise time is smaller and the oscillation frequency of the measured wave front is faster than the theoretical values due to very complicated reasons. On one hand, the loop inductance and load capacitance were estimated in a very conservative manner. Therefore, the inductance and resistance in the actual circuit might be lower. The inductance was experimentally measured to be approximately 190 nH, which is in good agreement with our estimate. However, the measurement was done at low voltage. As we know, spark inductance is not a constant. It is a function of the radius of the channel. Hence, spark inductance decreases with increasing voltage. As for parasitic capacitance, its value is very difficult to estimate or measure. Since the overall load capacitance is not very high, any error in its estimation has a significant impact on the calculated result. Another source of error is that various circuit parameters are treated as lumped parameters. Instead, they are distributive parameters affecting the waveform of the voltage output.

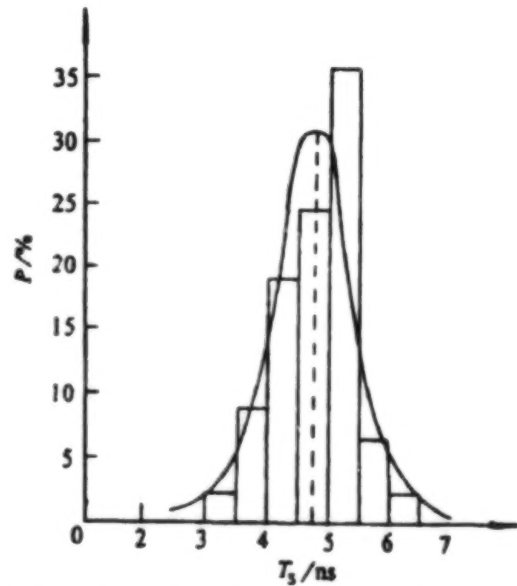


Figure 7. Statistical Result Histogram and Distribution of Probability Density of Waveform Rise-Time

The measured rise time shown earlier should also include the response time of the measurement system (primarily that of the high-voltage oscilloscope). This portion should be subtracted. The rise time of the 100 MHz oscilloscope is 3.5 ns. Hence, the actual rise time of the voltage output is

$T_r = (\bar{T}_r^2 - t_s^2)^{1/2} = (4.79^2 - 3.5^2)^{1/2} = 3.27$ ns. Therefore, we can claim that the rise time of this generator is less than 5 ns and the voltage output is over 160 kV. The original design objectives have therefore been exceeded.

References

1. Yang Dawei, et al., "Charging of High-Current Pulse Electron Accelerator," YUANZINENG KEXUE JISHU [ATOMIC ENERGY SCIENCE AND TECHNOLOGY], No 2, 1988, p 134.
2. Mishazi, T.A., "Formation of High-Voltage Nanosecond Pulse," Atomic Energy Publishing House, Beijing, 1975.
3. Feng Shiyao [7458 1597 7346], "Error Theory and Treatment of Experimental Data," Science Publishing House, Beijing, 1964.
4. Kalandalov, P.P., "Handbook of Induction Coefficients," Electric Power Industry Publishing House, Beijing, 1957.

3-cm Relativistic Backward-Wave Oscillator

92FE0732B Chengdu QIANG JIGUANG YU LIZI SHU [HIGH POWER LASER AND PARTICLE BEAMS] in Chinese Vol 4 No 2, May 92 pp 269-276

[Article by Li Jiayin [2621 1367 5255], Yu Shanfu [0060 0810 1133], Sun Jiahong [1327 0857 7703], Zhou Xiaolan [0719 2556 1526], Li Mingguang [2621 2494 0342] and Liu Shenggang [0491 4141 4854] of University of Electronic Science and Technology (UEST) of China, Institute of High-Energy Research: "Experimental Study of a 3-cm Relativistic Backward-Wave Oscillator"; MS received 10 Apr 91, Revised 15 Oct 91 (see early brief report in JPRS-CST-91-011, 31 May 91, p 2)]

[Text] Abstract

The principle of a relativistic backward-wave oscillator (BWO) is briefly discussed. The experimental apparatus and the measurement technique are described in detail. Preliminary experimental results are presented. The peak power of the relativistic BWO is approximately 98 MW and the efficiency is about 10 percent.

I. Introduction

In recent years, rapid progress has been made in the development of relativistic electron devices that produce high-power electromagnetic radiation via injection of an intense electron beam with energy more than several hundred keV and current over several kA. It is a product combining modern pulsed power technology with conventional microwave tube technology. Its advent provides a new possibility for solving a series of problems in microwave energetics, communications, plasma physics, medicine and high-power microwave technology. Relativistic microwave devices are classified based on different operating principles, such as relativistic wave devices, relativistic magnetron, relativistic gyrotron and virtual cathode oscillator. The first relativistic device developed was the relativistic BWO, which is also one of the most promising devices of the highest power. Researchers in the United States and

Russia began working on relativistic BWOs over two decades ago and the effort has never stopped. The 3-cm relativistic BWO developed by the Russians has a repetition frequency of 100 Hz and a peak power of 450 MW in continuous pulsing mode, with an efficiency as high as 20 percent.¹ The peak power of a 3-cm plasma-filled ripple boundary resonator (i.e., overmode BWO) is 15 GW. At 6.5 mm, it has reached 4.5 GW.² It is one of the highest power devices. Furthermore, because the relativistic BWO is simple in structure, can easily begin to oscillate, has a wide bandwidth and has high power, it is an important candidate for a portable high-power microwave source.

In the past two years, China began its experimental research on high-power relativistic devices. A year ago, we reported some preliminary experimental results with an 8-mm relativistic orotron.³ The power output was merely 10 kW back then. After improvements were made the power output of the device exceeded 6 MW. On the basis of that work, experimental work has been done using a 3-cm relativistic BWO; its power output is as high as 98 MW and the efficiency is approximately 10 percent. The basic principle, apparatus, test method and experimental results are briefly described in this paper.

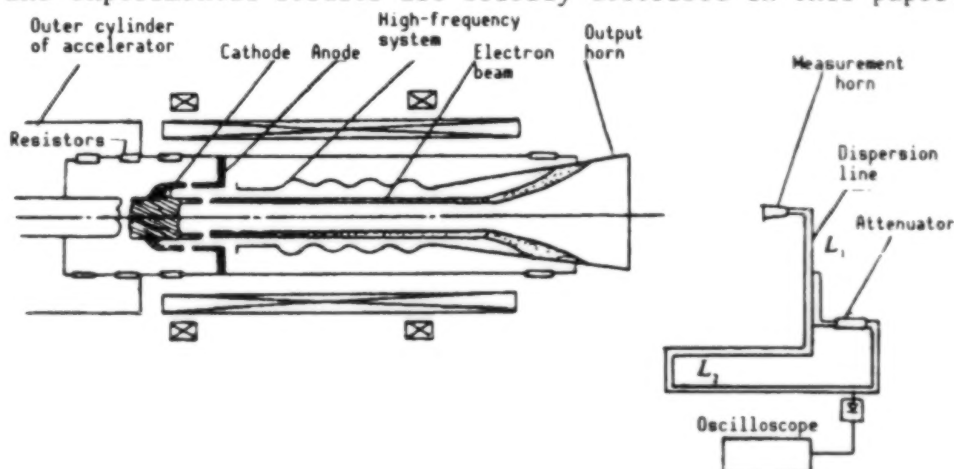


Figure 1. Experimental System and Outside View of Relativistic BWO

II. Basic Principle

Figure 1 shows the structure of the relativistic BWO. The slow-wave line is a weak corrugated waveguide. To the left is the over cutoff reducing waveguide and to the right is the output horn. The electron gun and the slow-wave line are placed in the solenoid magnetic field. The ring-shaped electron beam passes through the hole on the anode and the over cutoff waveguide to enter the interaction zone to interact with the electromagnetic wave in the slow-wave structure. It gives up a portion of its energy to the field. The beam is finally scattered and collected by the output horn.

The cross section of the weak wave rippled waveguide, i.e., the slow-wave line, can be described as follows:

$$R = R_0 + l \sin \frac{2\pi z}{d} \quad (1)$$

where R_0 is the mean radius of the waveguide, d is the spatial period of the ripple and l is the amplitude of the ripple. Theoretically, when $l < d^2/5R_0$, the basic wave traveling in the weak wave rippled waveguide is a fast wave⁴; its dispersion characteristics can be approximately expressed as those of a cylindrical waveguide with a radius R_0 :

$$\left(\frac{\omega}{c}\right)^2 = k_z^2 + k_1^2 \quad (2)$$

where c is the speed of light, k_z is the longitudinal wave number of the fast wave and k_1 is the transverse wave number. Due to the periodicity of the ripple waveguide, its characteristic modes can be expressed as follows:

$$E_z = \operatorname{Re}(\exp[i(\omega t + k_z z)] \sum_n E_{n,s} \exp(\mp i n \bar{k} z)) \quad (3)$$

where $\bar{k} = 2\pi/d$. Just as in any conventional BWO, the basic wave is propagating opposite to the direction of electron motion. Its negative primary spatial harmonic is synchronous with the electrons to achieve bunching and energy transfer. The synchronization condition is

$$\omega = k_z v_e = \bar{k} v_e \quad (4)$$

Different from a conventional BWO, the energy output is not from the end near the electron beam. Instead, it is reflected by the over cutoff reducing waveguide on the electron gun end and then goes out from the output horn. Since this reflected wave does not meet the synchronization condition, it has very little effect on the interaction process.

Figure 2 [not shown] is a Brillouin diagram of a relativistic BWO; when electron velocity v_e varies, working point A moves along the dispersion curve and the oscillation frequency also varies accordingly. This ensures the bandwidth and electron tuning characteristics of the BWO.

Conventional BWOs are low-to-medium-power devices under a few hundred watts. However, a relativistic BWO is a high-power device. There are inherent reasons. First, electrons in a relativistic BWO travel at a speed close to the speed of light c . This causes the transverse dimension of the attenuation of the synchronous harmonic field, L_1 , to increase:

$$L_1 = \frac{1}{|g_n|} = \beta_1 \gamma \frac{\lambda}{2\pi} \quad (6)$$

Here, λ is the free-space wavelength and $g_n \approx \frac{\omega}{c} (1 - \beta_1^2)^{1/2}$ is the transverse wave number of the synchronous harmonic waves. In a non-relativistic BWO, L_1 is very small and the field decays rapidly in the transverse direction. Hence, the synchronous harmonic wave is only a surface wave which only allows a thin layer of electrons to participate in the interaction. In a relativistic BWO, L_1 becomes larger and the field decays slower in the transverse direction. Its distribution extends from the surface into space to become a "body wave." Hence, a relatively thick electron beam is allowed to interact, which significantly increases the output power. Next, since a rippled waveguide is used instead of a slow-wave line, it significantly increases its mechanical strength and resistance to electric breakdown. Furthermore, since the dynamic voltage of a relativistic space-charge wave is $V = \gamma_0^3 v_1 v_0 / n_0$,⁵ the amount of electron velocity change caused by the same energy variation is much smaller than that in the non-relativistic case, which makes it easier to maintain the synchronization condition.

Based on the above description, a relativistic BWO is similar to a relativistic orotron in several aspects. However, because the energy flows in a different direction and the electron interaction space harmonic wave is different, the relation between its working frequency and the slow-wave structure period is also different. The two tubes also have different characteristics. The relativistic BWO is an electrically tunable wide-bandwidth device. The relativistic orotron is a narrow-bandwidth device whose frequency often varies due to mode discontinuity. The two devices have their own applications.

In the E mode, the starting oscillating current can be calculated according to the following⁴:

$$I_{st} = A \frac{mc^3}{e} \gamma^3 \beta^3 \frac{S}{L^2 Q} (I \rho_s)^{-2} \frac{k^2}{(k, \bar{k} - g^2)^2} \quad (7)$$

The oscillation starting time is

$$\tau = \frac{Q}{\omega} \frac{1}{(I/I_{st} - 1)} \ln \frac{E}{E_0} \quad (8)$$

where $A_{min} = 4.88$, $mc^3/e = 17$ kA, $\beta \approx \beta_1$, S is the transverse cross section of the slow-wave line, and L is the length of the slow-wave line. $Q = \omega L/v_g$, where v_g is the group velocity in the slow-wave line and ω is the angular frequency of the working wave. I is the actual working current. E and E_0 are the working strength and starting strength of the wave field, respectively.

III. Experimental Apparatus

The experimental system of the relativistic BWO is shown in Figure 1a. (Figure 1b shows the external appearance of the relativistic BWO.) Its major components include:

1. Pulsed Electron-Beam Source

In the first stage of the experiment, the EPA-74 pulsed linear accelerator of Southwest Institute of Applied Electronics was used. The voltage is tunable between 0.3-1.0 MV. The beam current is 10-15 kA and the pulse width is about 50 ns. The second stage of the experiment was done on the new pulsed linear accelerator at UEST. The operating voltage is 0.4-1.5 MV, beam current is 10-20 kA, and pulse width is ~70 ns.

2. Pulsed Magnetic Field

In order to achieve high interaction efficiency, the axis of the magnetic field is required to coincide with the geometric axis of the system. Furthermore, the magnetic field distribution needs to be flexibly adjustable along the axis in order to optimize the annular electron beam to get as close to the wall as possible. To this end, two sets of pulsed magnetic coils were made. Besides taking reliable measures to ensure symmetry with respect to the center, flexible adjustment of field distribution along the axis is made possible by using an auxiliary coil which moves along the axis and by altering the connection. The maximum magnetic field is 2-3 T and the rise time is 2.7 ms.

3. Electron Gun

A cold dual-cathode electron gun made of reactor-grade graphite is used. In a strong electric field, the burr on the cathode surface is vaporized by the intense-field-induced current to form a plasma. This kind of plasma can be considered to have infinite electron emission capability. The advantage of this type of cathode is that it has high current emission density. Moreover, it can be used repeatedly. The dual cathodes facilitate impedance matching which makes it easy to adjust the operating current of the BWO while the accelerator and diode are essentially matched. The working annular beam has a radius of $R_b \approx 7$ mm and the current is approximately 2 kA. Figure 3 [photograph not reproduced] is a picture of a plastic target damaged by the beam. Figure 4 is a computer-generated sketch of the dual-cathode electron gun showing the electrodes, equipotential lines and electron trajectories.

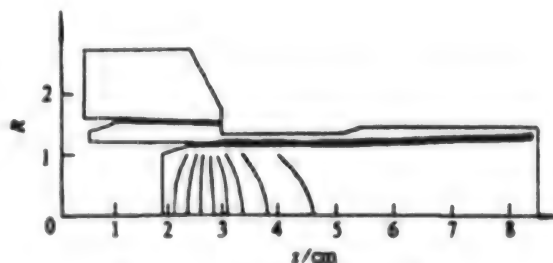


Figure 4. Electron Gun

4. High-Frequency System

This is a weak wave rippled waveguide. One end is connected to the over cutoff reducing waveguide and the other is connected to the output horn. In order to ensure effective interaction and minimize loss, the entire system is required to have excellent symmetry with respect to the center. The periodicity must meet certain requirements.

The device also must have satisfactory inner-wall roughness and electrical conductivity. In addition, in order to reduce the shielding effect of the tube wall on the pulsed magnetic field, the wall material should have higher resistivity. Or, it should be made of a very thin layer of highly conductive material. A model was made based on the basic parameters discussed above. Results of cold measurements taken are consistent with expected values. The basic wave propagating in the waveguide has a phase velocity of approximately 2 c. Figure 5 shows the cold measurement system of the high-frequency system. Figure 6 [photograph not reproduced] and Figure 7 are the frequency sweep and external appearance of the high-frequency system. (The strongest absorption peak corresponds to 10 GHz.)

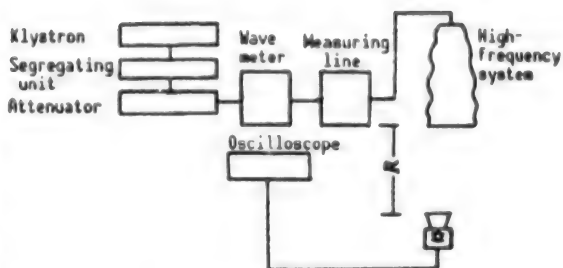


Figure 5. System for Cold Measurement

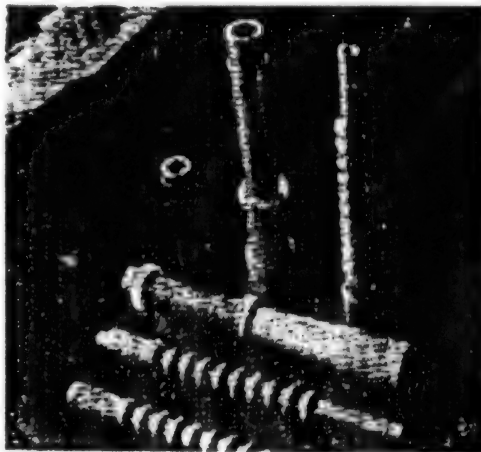


Figure 7. Outside View of Slow-Wave Structure and High-Frequency System

5. Testing System

The accelerator voltage and current are sampled by a voltage divider and a small shunt resistor, respectively, as shown in Figure 1. The results are displayed on a high-voltage oscilloscope. After the microwave signal emitted by the output horn is received by a measurement horn placed in a suitable position, it passes through a dispersion line of length L_1 . Then, it is split into two by a 3-dB directional coupler. One subsignal goes through a dispersion line of length L_2 and the other is attenuated after frequency doubling. They are recombined into one by means of a double-T connector. The signal is displayed and recorded on a high-speed oscilloscope after passage through a crystal detector. The dispersion line is made of a standard 3-cm-waveband waveguide. Waves of different frequencies travel at different velocities inside this dispersion line. The frequency, or wavelength, of the signal can be calculated from the time difference and the length of the dispersion line L_2 :

$$\lambda = \lambda_c \sqrt{1 - \left(\frac{L_2}{c\tau}\right)^2} \quad (9)$$

where λ_c is the cutoff wavelength of the dispersion line, c is the speed of light and τ is the time interval between the two signals. The power entering the measurement horn can be calculated as follows:

$$P_{i.th} = 2 \times 10^{-3} \left(\frac{d}{s} \right) \times 10^{[\alpha(L_1+L_2)/10 + A/10]} \text{ (W)} \quad (10)$$

where d is the signal amplitude (mV) read by the oscilloscope, s is the sensitivity of the detector (V/W), α is the attenuation coefficient of the dispersion line, and A is the overall attenuation of the series attenuator.

IV. Experimental Results

Due to existing constraints, we measured the wavelength and power received by the measurement horn, P_i (hot), by means of hot measurements. The operating mode and overall power were determined based on cold measurement results obtained from the same high-frequency system.

Figures 8 and 9 [photographs not reproduced] show the typical current and voltage waveforms.

Figure 10 [photograph not reproduced] shows an oscillogram of the output signal using a 7101A oscilloscope. Because the sampling interval of this digital storage oscilloscope is 20 ns, it is difficult to see the waveform in detail. Nevertheless, it is possible to determine that the dispersion signal is delayed by approximately 180 ns with respect to the reference signal. The length of dispersion line L_2 is 41.25 m. From equation (9), the frequency of radiation can be calculated to be $f \approx 10$ GHz.

The operating mode can be determined based on the radiation frequency and cold measurement results. With the cold measurement system shown in Figure 5, as well as a signal source of identical frequency to that obtained from hot measurement to excite the high-frequency system of the BWO, a low-power meter was used to measure the spatial distribution of radiation power by moving the measurement horn over a sphere of radius R_A and centered at the middle of the output horn. The result is shown in Figure 11. In the figure, P represents normalized power density. (Here, R_A is the distance between the centers of the two horns.) Based on the characteristics of a slow varying waveguide and the radiation pattern of an aperture antenna, the operating mode was determined to be E_{01} . Figure 12 shows the target pattern of E_{01} radiation measured by Russian scientists with a neon-filled tube.⁴ They are in excellent agreement.

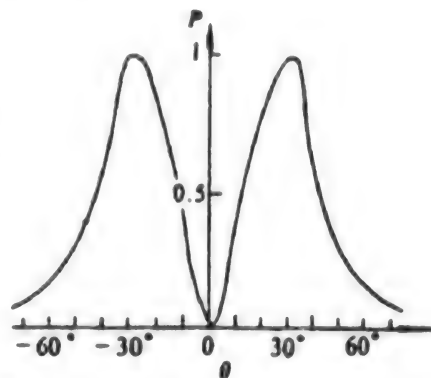


Figure 11. Space Distribution of Radiation Field

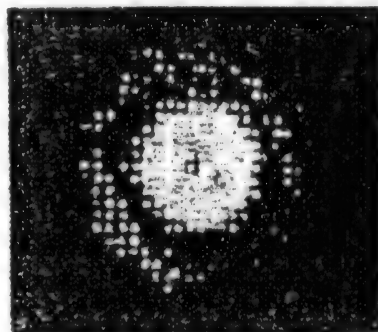


Figure 12. Visualization of the Field of E_{01} Mode From Reference 4

As a matter of fact, it is also possible to determine from the mode characteristics that the operating mode at $\lambda = 3$ cm has to be E_{01} in this case. Table 1 lists the circular waveguide radii corresponding to different cutoff modes at this wavelength.

Table 1.

Mode	H_{11}	E_{01}	E_{11}	E_{02}
Cut-off radius (cm)	0.879	1.146	1.829	2,636

Experimentally, the waveguide radius is $R_0 = 1.29$ cm. Only H_{11} and E_{01} were not cut off. Since there is no longitudinal electric field component in mode H_{11} and it is difficult to satisfy the synchronization and oscillation conditions at $\lambda = 3$ cm, therefore, the mode to get excited must be E_{01} . This is in complete agreement with cold measurement results. E_{11} and other higher modes may appear only when $\lambda < 2.12$ cm. Of course, since a rippled waveguide is not exactly the same as a smooth waveguide, it may be possible to have mode HE_{11} . However, this corresponds to a different wavelength. This issue will be discussed in more detail in a separate paper.

Once the operating mode is ascertained, it is possible to calculate the overall radiation power $P_{\Sigma,th}$ based on the power reception $P_{i,th}$ and other parameters obtained in hot measurements.

$$P_{\Sigma,th} = \kappa P_{i,th}$$

$$\kappa = P_{\Sigma,c}/P_{i,c}$$

where κ is the ratio of $P_{\Sigma,c}$ --which is the total power measured in a cold measurement when the high-frequency system and measurement horn and their relative position remain the same as in a hot measurement--to $P_{i,c}$, which is the power received by the measurement horn.

Two different methods were used to determine κ . They are considered as the upper and lower limit of κ . One is a direct measurement. Let the system shown in Figure 5 operate at a given frequency and measure the standing-wave ratio ρ . Then, the reflectance index is

$$|r| = \frac{\rho-1}{\rho+1}.$$

Replace the resonant cavity with a low-power meter to measure the power P_0 injected into the cavity. Assume that any mismatch is negligible. The power injected into the high-frequency system, P_{in} , can be calculated as follows:

$$P_{in} = P_0 (1 - |r|^2)$$

Neglect the loss in the slow-wave line, then $P_{\Sigma,c} = P_{in}$. The power entering the measurement horn, $P_{i,c}$, can be directly measured with a low-power meter under identical geometric conditions. Hence,

$$\kappa = P_0 (1 - |r|^2)/P_{i,c}$$

Because certain losses are neglected, the value of κ obtained is slightly high.

The other method is to integrate the measured field distribution over the entire space to obtain $P_{E,c}$:

$$P_{E,c} = \int_0^{\frac{\pi}{2}} d\theta \int_0^{2\pi} R^2 (\sin\theta) P_s(R, \theta, \varphi) d\varphi$$

R, θ, φ are the three coordinates of the spherical coordinate system with its origin located at the center of the radiation horn. $P_s = P_{i,c}/A_{ef}$ is the mean power density across an effective area A_{ef} of the receiving horn. Therefore,

$$\begin{aligned} \kappa &= \frac{P_{E,c}}{P_{i,c}} = \int_0^{\frac{\pi}{2}} d\theta \int_0^{2\pi} \frac{R^2 (\sin\theta)}{A_{ef}} \frac{P_i(R, \theta, \varphi)}{P_{i,c}} d\varphi \\ &= \int_0^{\frac{\pi}{2}} d\theta \int_0^{2\pi} \frac{R^2 \sin\theta}{A_{ef}} \tilde{P}_i(R, \theta, \varphi) d\varphi \end{aligned}$$

where $\tilde{P}_i(R, \theta, \varphi) = P_i(R, \theta, \varphi)/P_{i,c_{max}}$ is the relative power distribution. In the calculation, the integral is converted into a summation form which makes it difficult to obtain the total \tilde{P}_i covering the entire surface of the sphere with $R = R_A$. Furthermore, the area of integration does not cover the entire surface of the sphere other than the output horn. Hence, the value of κ obtained is generally low. A cross-check with these two methods indicates that the peak power is as high as 98 MW.

V. Conclusions

Preliminary experiments on the 3-cm relativistic BWO were successfully conducted. At $U = 450$ kV and $I = 1.8$ kA, a 98-MW power output was obtained at an efficiency of approximately 10 percent.

Acknowledgements

The authors wish to express their gratitude to Hu Kesong [5170 0344 2646], Chen Yutao [7115 5940 3447] and Deng Chaohui [6772 2600 6540] of Southwest Institute of Applied Electronics for their support and to Yang Zhonghai [2799 0022 3189], Wu Jianqiang [0702 1017 1730], Zhang Bing [1728 0393], Ma Wenduo [7456 2429 1122], Yang Ziqiang [2799 2737 1730] and Chen Xinyu [7115 2450 1342] for their assistance.

References

1. Korovin, S.D., et al., "Impulsno-periodicheski relativistskii karsinotron," Izv. Buzov, RADIOFIZIKA, Vol 29 No 10, 1986, p 1278.
2. Yuval Carmel, et al., "High-Power Microwave Generation by Excitation of Plasma-Filled Rippled Boundary Resonator," IEEE TRANS. PLASMA SCI., Vol 18 No 3, 1990, p 497.
3. Li Jiayin, Yu Shanfu, et al., "Experimental Study of an 8-cm Relativistic Orotron," QIANG JIGUANG YU LIZI SHU [HIGH POWER LASER AND PARTICLE BEAMS], Vol 2 No 1, 1990, p 114.
4. Bratman, V.L., et al., "Powerful Millimeter-Wave Generators Based on Stimulated Cerenkov Radiation of Relativistic Electron Beams," INTER. JOUR. OF INFR. & MILLI. WAVES, Vol 5 No 9, 1984, p 1311.
5. Liu Shenggang, "Theory of Relativistic Space-Charge Waves," DIANZI XUEBAO [ACTA ELECTRONICA SINICA], Vol 18 No 4, 1990, p 6.

High-Performance Short-Period FEL Wiggler

92FE0732C Chengdu QIANG JIGUANG YU LIZI SHU [HIGH POWER LASER AND PARTICLE BEAMS] in Chinese Vol 4 No 2, May 92 pp 314-318

[Article by Liu Qingxiang [0491 1987 1927], Zhou Chuanming [0719 0278 2494] and Hui Zhongxi [1920 6988 6932] of Southwest Institute of Electron Engineering, CAEP, P.O. Box 517, Chengdu 610003: "High-Performance Short-Period Wiggler"; MS received 24 Jun 91, Revised 15 Oct 91]

[Text] Abstract

The design of a high-performance short-period wiggler is described. Separate permanent magnets positioned in slots are used to realize half-period tuning of the magnetic field. Measurements made on a prototype wiggler show that the peak magnetic field $B_w = 0.35$ T and the maximum deviation of the magnetic field $\delta B_w/B_w < 1.25$ percent when the wiggler period is $\lambda_w = 10$ mm and spacing between magnets δ is 5 mm.

I. Introduction

The free electron laser (FEL) has many potential applications in scientific research and modern technology. However, existing FELs are cumbersome in size, complicated in structure and expensive to construct. These undesirable factors are seriously hampering the use of the FEL. Reducing the size of an FEL will make it more attractive. Based on the FEL resonance equation, $\lambda_s = \frac{\lambda_w}{2\gamma^2} (1 + a_w^2)$, where λ_s is the laser output wavelength, λ_w is the wiggler period, γ is the relativistic energy of the electron, $a_w = \frac{K}{\sqrt{2}}$, $K = 0.0934 \left(\frac{B_w}{kGs} \right) \cdot \left(\frac{\lambda_w}{cm} \right)$ and B_w

is the peak axial magnetic field of the wiggler. If the output wavelength λ_s is fixed, the required electron energy γ is lowered by reducing the wiggler period λ_w . Lowering the electron energy requirement also reduces the shielding requirements for X-rays and neutrons, which consequently lowers the complexity of the structure of the accelerator. Therefore, further investigation of short-period wiggler technology (i.e., the microwiggler) has a significant impact on the use of FELs in scientific research and modern technology. The microwiggler is being studied at the University of Maryland,¹ the Massachusetts Institute of Technology,² the University of California at Santa Barbara,³ the Brookhaven National Laboratory,⁴ the Los Alamos National Laboratory,⁵ and Stanford University. A 10-mm period hybrid wiggler made of NdFeB and A3 steel was used in this experimental study. The most recent results are presented in this paper. The second section describes the design of the microwiggler, the third section introduces the structural characteristics of the microwiggler, the fourth section contains the results and the fifth section is a discussion and analysis of the data.

II. Physical Design

A hybrid wiggler was first presented by Halbach⁶ in 1983. Figure 1 shows its principle of operation. We attempted to use such a structure to conduct our microwiggler study. The following issues were considered in the design.

2.1 Material Selection

Usually, the permanent magnet in a wiggler is either made of SmCo₅ or NdFeB. With a larger period-to-spacing ratio, NdFeB produces a magnetic field that is 20 percent higher than that of SmCo₅.⁷ Hence, we chose NdFeB as the material. There are a variety of soft magnet materials. However, most are based on high-saturation, high-conductivity vanadium permendure. We chose to use A3 steel as the soft magnet material.

2.2 Edge Configuration

Halbach analyzed three edge configurations,⁸ as shown in Figure 2. Based on Halbach's analysis, we selected the overhang configuration.

2.3 Thickness of Magnet

Obviously, with a fixed period, the thicker the permanent magnet is, the higher the center magnetic field it generates. From

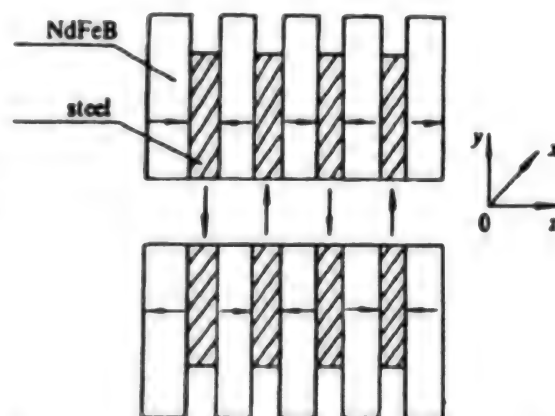


Figure 1. Schematic of Structure of Hybrid NdFeB + Steel Plane Periodic Magnet

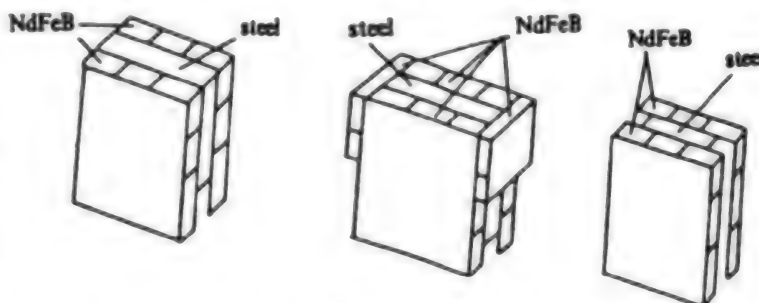


Figure 2. Schematic of Three-Edge Configurations for a Hybrid Wiggler

(1) flush; (2) w/side pieces; (3) w/overhang

this standpoint, the magnet ought to be as thick as possible. However, the thinner the soft magnet becomes, the stronger the harmonic component of the periodic distribution of the magnetic field is. This is undesirable. Besides, soft magnet becomes saturated when the permanent magnet is too thick. By taking these factors into consideration, a permanent-to-soft-magnet thickness ratio of 1.5:1 was chosen.

In conclusion, the permanent magnet chosen is 35 mm x 25 mm x 3 mm and the A3 steel soft magnet is 30 mm x 20 mm x 2 mm.

III. Structural Design

Normally, a hybrid wiggler is glued together. However, because of the short period, this method is impractical. The magnets cannot be easily stuck together and the error is substantial. Just as L. Elias pointed out, based on their

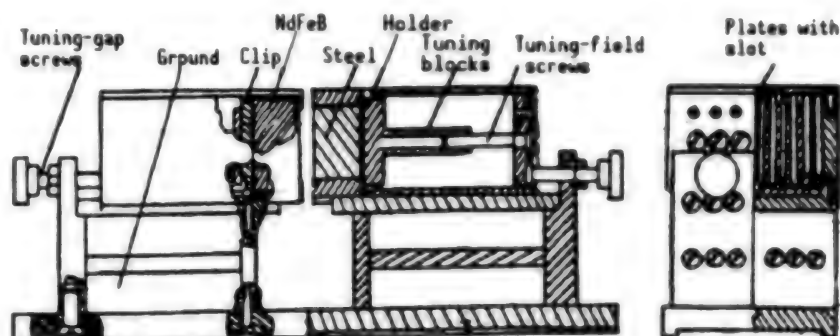


Figure 3. Mechanical Design of the Microwiggler

experience, it is impractical to construct a microwiggler using separate permanent magnets.⁴ Therefore, special consideration was given for the mechanical structure. We adopted a slot location method for position accuracy and ease of tuning. This arrangement makes it possible to use separate permanent magnets to develop a microwiggler.

As shown in Figure 3, the permanent magnet is held by a clip and the clip is also attached to the tuning block. The soft magnet is held in place by the permanent magnet and secured in place in the holder. The position of the permanent magnet can be adjusted by turning the fine-tuning screw to achieve half-period tuning of the magnetic field. Half-period tuning can improve the uniformity of the wiggler magnetic field. Furthermore, it provides a solid foundation for the design of variable-parameter devices, optical-cavity klystrons and wiggler inlets.

IV. Magnetic Field Measurement Results

A miniature Hall-effect probe with an effective area of 0.1 mm x 0.1 mm was used to measure the magnetic fields associated with the magnets and the microwiggler. Figure 4 shows the measurement circuit. The relation between control current I , output voltage V_0 and magnetic field strength B is $B = \frac{V_0}{kI}$, where k is the Hall coefficient of the probe. The current is in units of mA, voltage in mV and magnetic field B in T.

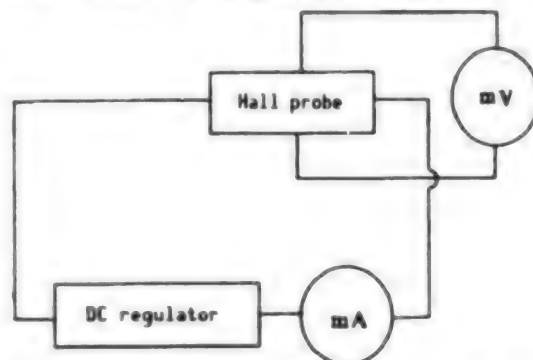


Figure 4. Principal Diagram of the Magnetic Measurements

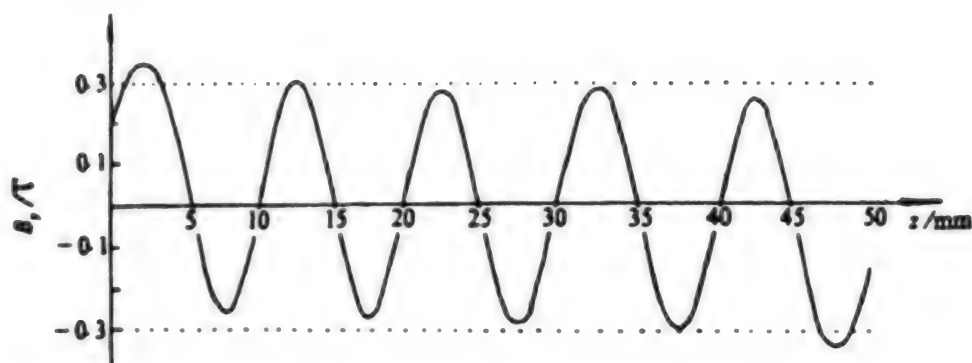


Figure 5. Regulated Five-Period Experiment Unit of Microwiggler, Magnetic Induction Intensity B_y on Axis of Unit Vs. z ($\lambda_w = 10$ mm, $\delta = 5.6$ mm)

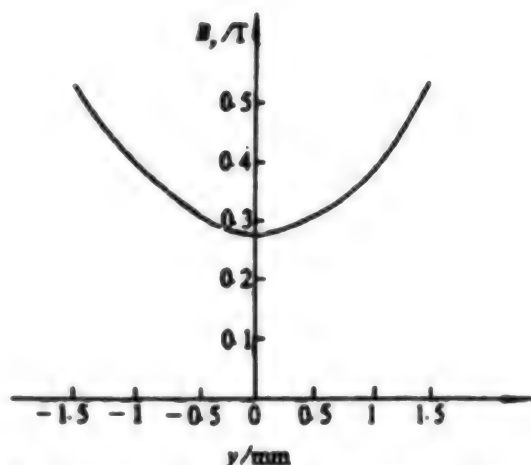


Figure 6. Regulated Five-Period Experiment Unit of Microwiggler, B_y/T on Axis of Unit Vs. y ; $\lambda_w = 10$ mm, $\delta = 5.6$ mm

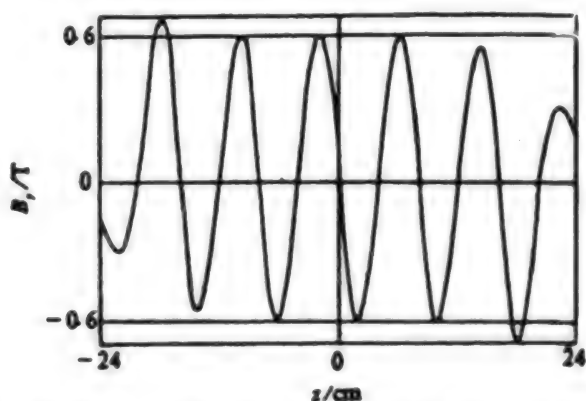


Figure 7. Magnetic Induction Intensity B_y/T on Axis of Experiment Unit of Wiggler Vs. z

Figures 5 and 6 show the magnetic field distributions obtained after initial testing. Compared to the results obtained with a hybrid wiggler designed by Q.C. Quimby, et al. (as shown in Figure 7), the magnetic field distribution shown in Figure 5 is in essential agreement. The differences are in the period magnitude and induction intensity. Nevertheless, the deviation of peak magnetic field in various periods is relatively large, i.e., approximately 3.2 percent, in this work. This is because the maximum deviation of the field of a single magnet is 25 percent.

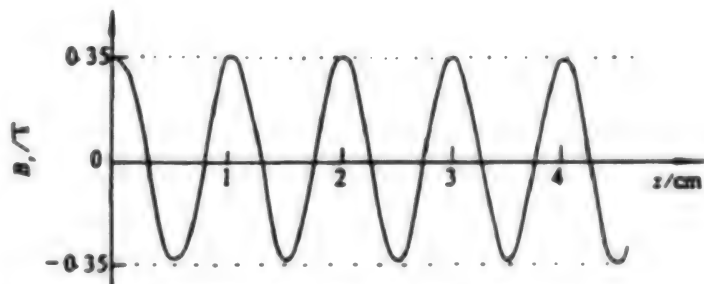


Figure 8. Magnetic Induction Intensity B_y on Axis of Five-Period Experiment Unit of Microwiggler Vs. z

Since the microwiggler has half-period adjustment capability, the final magnetic distribution curve (shown in Figure 8) was obtained after fine tuning. The deviation of peak magnetic field period-by-period was further reduced to approximately 1.7 percent. In addition, the terminal effect shown in Figure 5 is also resolved.

V. Discussion

A hybrid microwiggler (1 cm period) was used for the first time in an experimental study. This microwiggler produced a peak magnetic field of 0.35 T in a 5-mm gap. In addition, half-period tuning was achieved. By comparing our experimental data with results on existing microwigglers, this microwiggler has the highest peak magnetic field for comparable period and magnet spacing ratio, as shown in Table 1. Its half-period tunability is even more attractive. We have employed this structure to construct a 50-period microwiggler (1 cm period) that is now being tested. We plan to drive this microwiggler with a low-energy electron beam to perform FEL experiments. However, considering electron-beam and light-beam transport, the magnetic field of this microwiggler needs to be further raised. On the basis of this hybrid structure, we have already presented a modified structure. Its magnetic field intensity can be 10 percent higher than that of a conventional hybrid structure. This novel permanent magnet microwiggler will be discussed in a separate paper.

Table 1. Comparison Among Results of Microwiggler Experiments

	Type	Period λ_w/mm	Space δ/mm	Peak mag- netic induction intensity B_w/T	$\frac{\delta B_w}{B_w}$	Tun- able- ness
Univer- sity of Maryland	Electromagnet, planar polarization	5.4-15	2.2-7	0.2	5%	No
MIT	Electromagnet, planar polarization	10.2	5.1	0.32*	1%	Yes
Santa Barbara	Permanent magnet, planar polarization	4	2.2	0.12	2.76%	No
Los Alamos	Electromagnet, circular polarization	8.5	2.2	1	/	No
CAEP	Hybrid magnet, circular polarization	10	5	0.35	1.7%	Yes

* Treated by low-temperature cooling, peak value of magnetic induction intensity can be reached in 0.5 T.

**This value is r.m.s.

References

1. Destter, W.W., J. APPL., Vol 60 No 2, 1986, p 15.
2. Chenn, S.C., APPL. PHYS LETT, Vol 54 No 14, 1989, p 1299.
3. Batchelor, K., NUCLEAR INSTRUMENTS AND METHODS IN PHYSICS RESEARCH, Vol A296, 1990, pp 239-243.
4. Elias, L.R., Ibid., Vol A293, 1990.
5. Warren, R., Ibid., Vol A296, 1990.
6. Halbach, K., JOURNAL DE PHYSIQUE, Vol 44, 1983, p C1-211.
7. Billaraon, M., Ibid., p C1-29.
8. Quimby, D.C., NUCLEAR INSTRUMENTS AND METHODS IN PHYSICS RESEARCH, Vol A272, 1988, pp 192-198.
9. Halbach, K., IEEE TRANSACTIONS ON NUCLEAR SCIENCE, Vol NS-32 No 5, 1985, p 3640.
10. Kim, S.H., Ibid., p 2386.

Design of Electron Optical Column for DJ-2 Variable-Rectangle E-Beam
Lithography System With 0.2-Micron Edge Resolution

92FE0510A Beijing DIANZI KEXUE XUEKAN [JOURNAL OF ELECTRONICS] in Chinese
Vol 14 No 2, Mar 92 pp 176-183

[Article by Kang Niankan [1660 1819 0974] of the Institute of Electronics of
the Chinese Academy of Sciences: "Electron Optical Design of DJ-2 Variable-
Rectangle E-Beam Lithography System"; MS received 30 Mar 91, revised
17 Jun 91]

[Text] Abstract

The electron optical design of a variable-rectangle electron-beam (e-beam) lithography machine is discussed with emphasis on the analysis of optical path configuration and shape deflection compensation. The DJ-2 system employs a minimum number of lenses to meet the requirements for variable spot shaping. In order to achieve high-speed shape deflection, a high-sensitivity electrostatic deflector with series-connected flat plates is used. By means of precise linear and rotational compensation, the spot current density, edge resolution and position of spot origin remain unchanged when the spot size varies. It has been experimentally demonstrated that with a tungsten hairpin cathode, the spot current density is 0.4 A/cm^2 and the edge resolution is better than $0.2 \mu\text{m}$ within a $2 \times 2 \text{ mm}$ scan field.

I. Introduction

As the density of VLSI becomes higher, its primary fabrication technique, e-beam lithography, is also being developed and perfected. One of the major breakthroughs is that it is possible to use a variable rectangular beam to replace the conventional Gaussian beam.¹⁻³ As a result, the speed is increased so substantially that an e-beam lithography system becomes a piece of production equipment in the microelectronics industry.

The optical configuration of a variable-rectangle e-beam lithography unit is far more complicated than its Gaussian-beam counterpart because there are two different but interrelated electron images -- i.e., the image of the electron source (source image) and the image of the grating (object image) -- in the system at the same time. Optically, these two images

must be effectively separated to the extent that each image can be independently adjusted. In order to have the same line pattern clarity for different spot sizes, it is necessary to ensure that the spot current density, edge resolution and spot origin remain unchanged when the spot size varies. This requires accurate computation in the design of the optical path. In addition, in order to obtain uniform exposure patterns, the current density within the spot must be as uniform as possible. Hence, the grating must be illuminated uniformly. This paper describes the electron optical column we developed for the DJ-2 variable-rectangle e-beam lithography system. Some key issues in the electron optical design are discussed and analyzed and some experimental results are presented.

II. Design of the Electron Optical Column

1. Optical Path Structure, Computation of Its Electron Optical Properties

The electron optical specifications of the DJ-2 variable-rectangle e-beam lithography system are given in Table 1. The optical configuration of the corresponding column is shown in Figure 1. An e-beam emitted from a triode gun (G) with a tungsten hairpin cathode uniformly illuminates the rectangular grating A_1 . A 1:1 image of A_1 is formed on the plane of the second rectangular grating A_2 by lens L_1 . By varying the voltages on the shape deflector plates (D_x and D_y) between A_1 and A_2 , the image of A_1 can be moved on A_2 to obtain the spot size required, such as the dark rectangle shown on the right side of the figure. Auxiliary deflectors D_x' and D_y' at L_1 are used to keep the source image (S_1) from shifting off axis due to deflection in order to maintain the spot current density, edge resolution and spot origin constant. After shrinking the image by a factor of approximately 1/10 with lens L_3 , which is a composite of A_1 and A_2 , a focused image is formed on target T by lens L_4 . In order to intersect larger-beam-angle and nonuniform-current-density electrons at the edge, a circular grating, A_0 , which is slightly larger in diameter than the electron source image S_3 , is placed at the center of L_4 . The position of the spot on the target is controlled by the deflector system D_0 behind the lens. Since the required deflector field is small, a simple electrostatic plate deflector is chosen. Its advantage is that the same deflector can be shared by the highly accurate deflection (2 mm) provided by the main field and the high-speed deflection (100 μ m) provided by the auxiliary field, instead of the conventional approach which requires electromagnetic deflection and electrostatic deflection separately. Of course, deflection behind the lens lengthens the working distance of the system. Consequently, objective lens aberration is also larger. This design is only applicable to smaller beam angles, which limits the current density attainable on the target. Other important elements in the column include electron-gun coaxial coils AC_1 and AC_2 , beam gate B which controls the beam according to the pattern, Faraday cup F for beam current detection, coaxial scanning coil SC, rotating lens RL which fine-tunes the orientation of the rectangular spot in the direction consistent with the movement of the platform, and stigmator ST.

Table 1. Electron Optical Specifications of the DJ-2

Beam current density	0.4 A/cm ²
Spot size	1-12.5 μm rectangle, in 0.05 μm steps
Edge resolution	0.2 μm
Scan field dimensions	2 x 2 mm ²

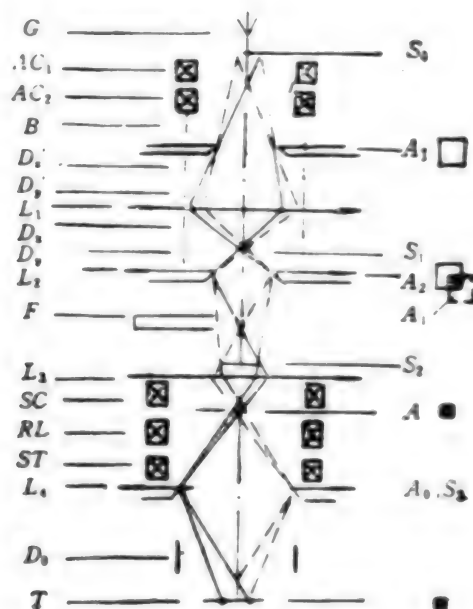


Figure 1. Optical Configuration of the DJ-2 Electron Optical Column

A unique feature of the optical path shown in Figure 1 is that it employs the least number of lenses to meet the requirements of the variable-rectangle e-beam lithography system. Hence, the overall length of the lenses is shorter. This not only facilitates coaxial adjustment but also reduces the loss of resolution caused by the space-charge effect of the e-beam (see equation (1)). Some variable-rectangle lithography systems employ one (e.g., JBX-6A⁴ and EB55⁵) or even two (e.g., VL-R2⁶) focusing lenses in their optical configurations to adjust the illumination on the imaging grating (object). This kind of arrangement increases the overall length of the lenses and further complicates its structure. In a variable-rectangle lithography system, the magnitude of the current density corresponding to a uniform spot on the target is determined by the brightness of the electron source and its emissivity (which is the product of the spot diameter and the divergence angle of the beam), as shown in equation (6) below. According to the principle of invariance of e-beam brightness and the Lagrange-Helmholz theorem, these two quantities will not increase because of focusing

lenses. This unique feature associated with the variable-rectangular beam is different from the case of a Gaussian beam where the primary design objective is to obtain the peak current density on the axis. Current fluctuations caused by dimensional discrepancies of the electron-gun structure can be compensated by adjusting the gate bias of the electron gun, instead of using a focusing lens. From the standpoint of e-beam radiation, the uniform current density attainable on the target surface is limited by the electron source. Most e-beam devices use either a hairpin tungsten cathode or a LaB₆ cathode. Although a LaB₆ point cathode typically has a higher brightness, its cross spot diameter and divergence angle are much smaller than those of the tungsten cathode. It is difficult to provide uniform illumination across a large-area grating. Furthermore, the fabrication of a plateau-shaped LaB₆ cathode, which is more suitable for a variable-rectangle lithography system, is very complicated. Therefore, we selected a tungsten cathode of a relatively thicker diameter in this work. Although its brightness is relatively low, its divergence angle is large. The uniformity across the rectangular grating is as high as 99 percent.

Another unique feature of the optical path shown in Figure 1 is that the position of the second rectangular grating A₂ coincides with the main plane of the second imaging lens L₂. With such an arrangement, when effectively uniform illumination is achieved by adjusting the excitation of L₂ so that the secondary image of the intermediate image S₁ of the electron source is formed at the pupil of reducing lens L₃, the image of the rectangle produced by the two rectangular gratings will not be affected. Hence, this configuration can effectively separate the source image from the object image to allow the system to operate in its optimal working condition.

The electron optical characteristics of the optical path shown in Figure 1 have been calculated in detail.⁷ Table 2 shows the primary optical characteristics obtained. Table 3 lists the third-order chromatic aberration and first-order astigmatism data. Table 2 also shows the relative errors between calculated and experimental values. Figure 2 shows the calculated beam spot at the corner of the deflection field. It demonstrates that the optical configuration satisfies the resolution requirement shown in Table 1.

Table 2. Comparison of Calculated Primary Optical Characteristics With Experimental Data

Characteristic parameter		Calculated value	Experimental value	Error (%)
Overall amplification		-0.0943	0.10	6.04
Lens excitation (AT)	Imaging lens	576.7620	563	2.26
	Focusing lens	785.000	768	2.17
	Reducing lens	737.9273	736	0.26
	Objective lens	617.4350	641	3.82
Main deflector voltage (V)	X deflection 1 mm	39.2490	39.57	0.82
	Y deflection 1 mm	40.3834	38.69	4.19
Angle of inclination of beam on target at the edge of the deflection field (°)	X	0.4658	--	--
	Y	0.5589	--	--

Table 3. Calculated Values of Third-Order Geometric Astigmatism and First-Order Aberration (Unit: μm)

Type \ Source	Axial	Deflection	Imaging beam spot	Mixed	Total
Spherical aberration	0.074	--	--	--	0.074
Isotropic coma aberration	--	0.004	0.000	--	0.004
Anisotropic coma aberration	--	-0.004	0.000	--	0.004
Curvature of field	--	0.058	0.001	0.000	0.058
Isotropic astigmatism	--	0.034	0.001	0.000	0.034
Anisotropic astigmatism	--	0.045	0.000	0.000	0.045
Isotropic distortion	--	0.056	0.002	0.001	0.057
Anisotropic distortion	--	0.087	0.000	0.001	0.088
Axial color aberration	-0.059	--	--	--	0.059
Lateral color aberration	--	-0.141	0.002	--	0.141
Overall aberration	0.094	0.163	0.003	0.000	0.188

E-beam parameters as follows: voltage 20 kV, beam half-angle 1.85 mrad, deflection field $2 \times 2 \text{ mm}^2$, imaging spot size $10 \times 10 \mu\text{m}^2$, beam voltage fluctuation 2 V.

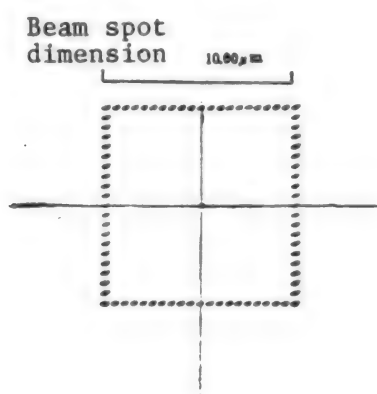


Figure 2. Beam Spot at the Corner of the Deflection Field on Target ($\pm 1 \text{ mm}$)

In addition to aberrations, there are a few other factors that affect the ultimate resolution of a variable lithography system. First, compared to a Gaussian-beam system, the beam current of a variable-beam system is much higher, usually by 3-4 orders of magnitude. (The former is of the order of nanoamperes while the latter is of the order of milliamperes.) Hence, the space-charge effect (Boersch effect) associated with a variable-beam lithography system is far more severe. Especially when the beam spot is large, this effect cannot be neglected. Based on an analysis done by Crewe,⁸ the edge fuzziness caused by space charge, $\delta_{sc}(\mu\text{m})$, is proportional to the current density $I(\text{A})$ and the image-to-object distance $l(\text{cm})$, and it is inversely proportional to the e-beam half-angle α (rad) and the $(3/2)$ power of the beam voltage $V(\text{V})$, i.e.,

$$\delta_{sc} = \sum_i \frac{l_i I}{\alpha_i V^{1/2}} \times 10^4 \quad (1)$$

In the optical path shown in Figure 1, l_1 includes three parts, i.e., l_1 , which is the distance between A_1 and A_2 ; l_2 , which is the distance between A_2 and A ; and l_3 , which is the distance between A and T . Let the beam half-angles and magnification factors associated with the imaging lens, reducing lens and objective lens be α_1 , α_2 , α_3 , and M_1 , M_2 , M_3 , respectively. Then, we have

$$\delta_{sc} = [(\alpha_1/\alpha_3)^2 + (\alpha_2/\alpha_3)^2 + (\alpha_3/\alpha_3)^2]^{1/2} (I/V^{1/2}) \times 10^4 \quad (2)$$

Since $\alpha_2 = \alpha_1/M_1$, $\alpha_1 = \alpha_2/M_2 = \alpha_3/(M_2 M_3)$, we get

$$\delta_{sc} = [(M_2 M_3/\alpha_3)^2 + (M_3/\alpha_3)^2 + 1]^{1/2} [I/(\alpha_3 V^{1/2})] \times 10^4 \quad (3)$$

With a given set of optical parameters (M , α , l), in order to keep δ_{sc} below the resolution requirement, the value of I must be limited. This means that the product of current density and spot area must be less than a certain value.

Next, as discussed earlier, the uniform illumination of a rectangular grating is limited by the emissivity of the electron gun. Based on the Lagrange-Helmholtz theorem,

$$d_g \alpha_g = d_t \alpha_t \quad (4)$$

where d_g and α_g are the diameter of the cross spot of the electron gun and the beam divergence half-angle, respectively, and d_t and α_t are the spot diameter and beam half-angle on the target, respectively. In order to keep the current density uniformity at above 90 percent, the emissivity of the electron gun E has to meet the following requirement:⁶

$$E = d_g \alpha_g > \sqrt{2} b \alpha_t \quad (5)$$

where b is the maximum spot size required. Hence, the spot current density, which is limited by the emissivity of the electron gun, becomes

$$J_s = \beta \pi \alpha_t^2 \leq (1/2) \pi \beta (d_g \alpha_g / b)^2 \quad (6)$$

where β is the brightness of the electron gun.

Finally, the high-speed variable-shape deflection requirement imposes some constraints on the maximum output and digits of the digital-to-analog (D/A) conversion of the deflector. Consequently, the maximum spot size associated with a certain resolution (step) is limited. Based on the 0.05 μm resolution requirement shown in Table 1, with 8-bit D/A, the maximum spot size allowed is $0.05 \times 2^8 = 12.8 \mu\text{m}$.

In addition, the effect of other factors on current density and edge resolution, such as charge and discharge inside the lenses, external electromagnetic interference, mechanical vibration and heating of the corrosion inhibitors, is hard to estimate quantitatively. The effect of the four limiting factors discussed above is plotted to define the working area in the column, as shown in Figure 3.

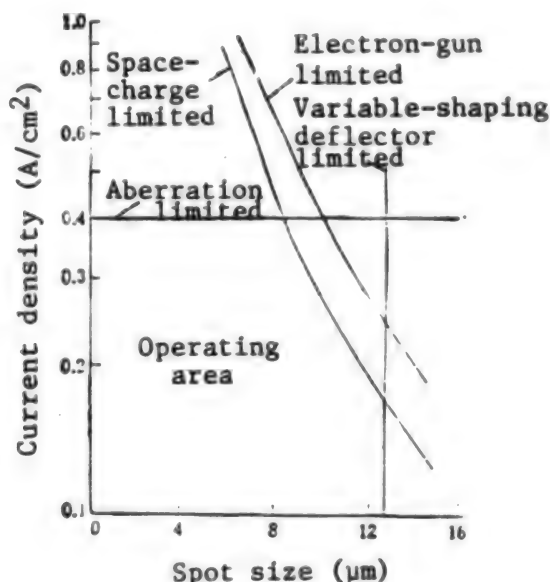


Figure 3. Working Area in the Column as Determined by the Factors Limiting Current Density and Spot Size (Area surrounded by thick solid lines)

2. Design of the Imaging Deflector⁹

A key issue in the electron optical design of a variable-beam lithography system is to ensure that the current density, edge resolution and spot origin on the target surface remain unchanged as spot size varies. There are some problems associated with the design of other optical configurations. For instance, EB55⁵ and HL600¹⁰ do not take any shaping deflection compensation measures. The shape-varying optical path only approximately satisfies the condition to produce an image of the first imaging grating on the plane of the second imaging grating. The displacement of the source image in the direction perpendicular to that of electrostatic deflection caused by the leakage of the magnetic field of the imaging lens to the deflector is minimized in these two systems by placing the imaging system symmetrically with respect to the geometric centers of the two lenses and by exciting the two lenses in opposite phases. This arrangement imposes unnecessary constraints on the optical design. Furthermore, it is very difficult to completely eliminate shift of source image. Hence, it ultimately affects its resolution. Although shape-deflection compensation measures have been taken in JBX-6A,⁴ that system is not perfect. Sometimes, spot origin shift is produced by improper compensation. Other variable

lithography systems employ quadrupole or octopole deflectors.^{1,11} Although deflection compensation is made easier, deflection sensitivity is reduced due to increased distance between poles; this makes it more difficult to construct deflection amplifiers.

Based on an analysis of existing variable optical configurations, the DJ-2 system employs a high-sensitivity electrostatic imaging deflector with series-connected parallel plates, as shown in Figure 4. In order to keep the source image position constant while spot size varies, in addition to the main imaging deflector plates, D_x and D_y , another pair of compensation deflector plates, D_x' and D_y' , are placed above the imaging lens L . Let us assume that the deflection of A_1 and the A_2 plane is d_{square} . Then, the deflection angle due to the main plates is:⁹

$$\alpha = \frac{d_{\square}}{l_s} \left(1 + \frac{m_0 l_s l'_s}{m_s l_s l'_{s2}} \right) \quad (7)$$

where m_0 and m_{square} are the amplification factors of the electron source and rectangular grating due to L . The corresponding compensation deflection angle is

$$\alpha' = \alpha l_s / (m_s l'_{s2}) \quad (8)$$

The ratio of α' to α is defined as the linear compensation factor η , i.e.,

$$\eta = \alpha' / \alpha = l_s / (m_s l'_{s2}) \quad (9)$$

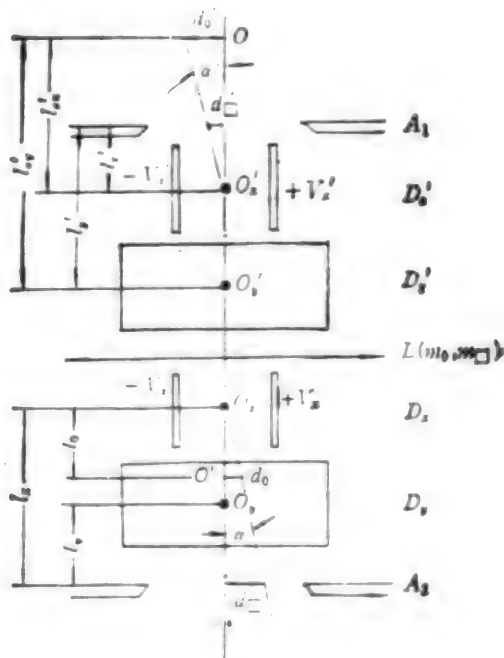


Figure 4. Optical Configuration of the Imaging Deflector

The above equation is valid only when the direction of deflection of the compensation plates is consistent with that of the main plates. Since the two sets of deflection plates are placed on both sides of the shaping lens, when the relative mechanical rotation angles of the two sets of deflector plates are not equal to the rotation angle of the lens, or when main plate X is not perpendicular to main plate Y, or when transverse deflection caused by leakage of the lens magnetic field exists, rotational compensation is required to keep the source image on the axis. Figure 5 illustrates the direction of deflection on a cross section containing the source image and perpendicular to the optical axis. O is the optical axis, D_x and D_y are the two deflection directions of the main-plate orthogonal, and D_x' and D_y' are the directions of deflection of the compensation plates after going through L. The difference is an angle β . Assume source image O is shifted to point A along D_x due to the main plates during shaping and the length of OA is d_0 . Also assume that there is an additional displacement AB in the Y direction because main plate Y is not perpendicular to main plate X or because there is magnetic field leakage on this cross section. The resultant deflection is OB. Its angle with respect to D_x , γ , is equal to the deviation from orthogonality between Y and X. With the angle between the combined deflection due to magnetic field leakage and D_x , it is not difficult to find that the rotation angle for compensation plate X should be

$$\alpha'_x = d_0 / \cos \gamma \cdot \cos(\beta + \gamma) / (m_x l'_{xx}) \quad (10)$$

Correspondingly, the rotation angle for compensation plate Y should be

$$\alpha'_y = d_0 / \cos \gamma \cdot \sin(\beta + \gamma) / (m_y l'_{yy}) \quad (11)$$

The rotation compensation factor, η_r , is the ratio of α'_y to α'_x :

$$\eta_r = \alpha'_y / \alpha'_x = l'_{xx} / [l'_{yy} \tan(\beta + \gamma)] \quad (12)$$

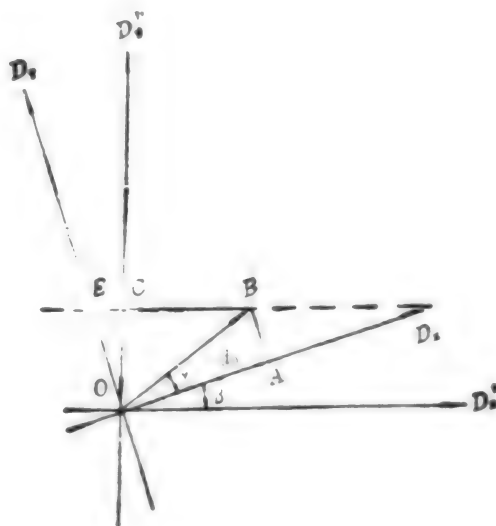


Figure 5. Deflection Direction of Source Image on a Cross Section Perpendicular to the Optical Axis

The rotational compensation discussed above is accomplished through the use of compensation plates, i.e., to deflect B to C along D_x' and then move C back to O along D_y' . In principle, it is also possible to apply the compensation signal to the main plate Y itself, i.e., to deflect B to E along D_x' and then push E back to O by the voltage applied to Y. However, $OC \leq OE$, i.e., it requires more deflection by means of main plate Y as compared to compensation plate Y. In addition, from Figure 4 ($OO_y' \gg O'O_y$) it is obvious that the main plates have a much lower source image deflection sensitivity compared to that of the compensation plates. Hence, the latter approach is not desirable. When source image O' is very close to O_y , the geometric center of main plate Y, or when they coincide with each other, rotational compensation becomes impossible. This is why some variable-lithography systems that employ this kind of compensation scheme cannot keep the spot on the target constant.

Experimental observation shows⁹ that the imaging deflection compensation scheme employed in DJ-2 has met all design requirements for the variable optical configuration. The beam current density, edge resolution and spot origin position remain constant, independent of spot size.

III. Experimental Testing and Results

1. Spot Testing Method

Since the variable optical configuration is very complex and the spot shape is "anisotropic," a suitable method is required to determine its characteristics. Initially, in order to investigate the entire optical configuration, the spot was directly observed cross-section-by-cross-section along the optical axis by using the electromagnetic amplification system under the main lens column. By monitoring the patterns associated with the charge and discharge of the e-beam and external interference, it is possible to identify the locations that cause contamination and interference. Furthermore, it is also possible to observe the deflection and electron optical coaxial effect of the lenses and deflectors. Hence, direct observation is an effective experimental technique to determine the characteristics of the column. This can relatively quickly make every component function normally. Moreover, it can be used to determine certain major parameters of the e-beam in a semi-quantitative manner. Based on the results, the column can be placed on a precision laser platform. A cross-hair scan method⁴ is then used to measure the rapidly varying e-beam parameters, such as rectangular spot size, spot orientation, beam current density, edge resolution, deflection field dimensions and field distortion. Adjustments and calibrations are made based on the data acquired until the accuracy requirement of exposure is satisfied. This technique can provide rapid verification of spot parameters during exposure, which shortens processing time.

2. Experimental Results

Figure 6 [photograph not reproduced] shows the waveforms of the beam current and its first and second derivatives. It shows that at different spot sizes the current densities are identical and the current distribution is uniform.

The maximum current density is over 0.4 A/cm^2 and the edge resolution has met the $0.2 \text{ }\mu\text{m}$ requirement. Figure 7 [photograph not reproduced] shows lithographic patterns obtained with different spot sizes. The patterns remain uniform with rectangular spots varying from 1-12.5 μm . Figure 8 [photograph not reproduced] is a pattern of an IC lead plate.

IV. Conclusions

The electron optical design of the DJ-2 variable-rectangle e-beam lithography system meets the functional requirements with the least number of lenses. Its optical configuration is sound. In order to keep current density, edge resolution and spot origin position constant with various spot sizes, precision linear and rotational compensations are introduced to the high-sensitivity electrostatic deflector using series-connected parallel plates to solve several problems caused by variable spot size. It has been experimentally demonstrated that the spot size can be independently varied in $0.05 \text{ }\mu\text{m}$ steps between 1 and 12.5 μm . The maximum current density is over 0.4 A/cm^2 and the edge resolution is better than $0.2 \text{ }\mu\text{m}$ in a $2 \times 2 \text{ mm}$ scanning field.

This work is a part of the "variable-rectangle electron-beam lithography system" program in the Seventh 5-Year Plan. The author wishes to thank Huang Lanyou [7806 5695 0645], Jiang Junji [3068 6874 1015], Zhu Xieqing [2612 0588 0615], Wu Mingjun [0702 2494 0971], Wu Wei [0702 0251], and Tong Liangfa [4547 5328 4099] for their participation in this work and Gu Wenqi [7357 2429 3825], Wang Liming [3769 3810 2494], and Fang Guangrong [2455 0342 2837] for their assistance in the testing stage.

References

1. H. C. Pfeiffer, J. VAC. SCI. TECHNOL, Vol 15, No 3, 1978, pp 887-890.
2. J. Trotel, J. VAC. SCI. TECHNOL., Vol 15, No 3, 1978, pp 872-873.
3. E. Goto et al., J. VAC. SCI. TECHNOL., Vol 15, No 3, 1978, pp 883-886.
4. G. Cogswell et al., "Electron Lithography System With Variable-Shaped Electron Beam," Proc. 8th International Conference on Electron and Ion Beam Science and Technology, Seattle, USA, 1978, pp 117-133.
5. N. Saitou et al., J. VAC. SCI. TECHNOL., Vol 18, No 4, 1981, pp 1087-1093.
6. M. Nakasuji et al., J. VAC. SCI. TECHNOL., Vol 19, No 3, 1982, pp 872-878.
7. H. C. Chu et al., OPTIK, Vol 61, No 2, 1982, pp 121-145.
8. A. V. Crewe, OPTIK, Vol 52, No 4, 1978, pp 337-346.
9. Kang Niankan et al., DIANZI KEXUE XUEKAN [JOURNAL OF ELECTRONICS], Vol 12, No 2, 1990, pp 161-168.

10. N. Saitou et al., J. VAC. SCI. TECHNOL., Vol B3, No 1, 1985, pp 98-101.
11. R. D. Moore et al., J. VAC. SCI. TECHNOL., Vol 18, No 4, 1981, pp 950-952.

- END -

END OF

FICHE

DATE FILMED

23 Oct 1992